LANGMUIR Article
Cite This: Langmuir 2018, 34, 4314−4323
pubs.acs.org/Langmuir

Molecular Dynamics Modeling of Methylene Blue−DOPC Lipid Bilayer Interactions

Nazar Ileri Ercan,[†,‡,§] Pieter Stroeve,[†] Joseph W. Tringe,[‡] and Roland Faller*[,†]

[†]Department of Chemical Engineering, University of California Davis, One Shields Avenue, Davis, California 95616, United States
[‡]Lawrence Livermore National Laboratory, 7000 East Avenue, Livermore, California 94551, United States
[§]Chemical Engineering Department, Bogazici University, Bebek, 34342 Istanbul, Turkey

Supporting Information

ABSTRACT: We present a coarse-grained MARTINI model for methylene blue (MB) and investigate the interactions of MB with dioleylphosphatidylcholine (DOPC) lipid bilayers by molecular dynamics simulations. Our results show that the charge state of MB and the oxidation degree of the DOPC bilayer play critical roles on membrane properties. Oxidation of the DOPC bilayer significantly increases permeability of water and MB molecules, irrespective of the charge state of MB. The most significant changes in membrane properties are obtained for peroxidized lipid bilayers in the presence of cationic MB, with ∼11% increase in the membrane area per lipid head group and ∼7 and 44% reduction in membrane thickness and lateral diffusivity, respectively.

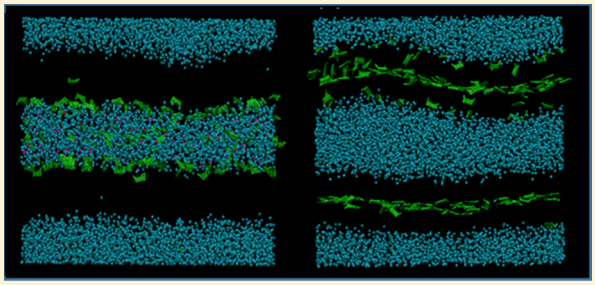

INTRODUCTION

Methylene blue (MB), also known as methylthioninium chloride, is a cationic phenothiazinium dye and an efficient photosensitizer that is extensively used for staining[1] and medical purposes.[2] In particular, it has promising uses in photodynamic therapy (PDT) of tumors[3−6] and microbial infections[7−9] because of its light absorbing property,[10] its ability to produce singlet oxygen in high yields,[10] and its affinity to mitochondria[11,12] which facilitate cell apoptosis. A promising therapeutic approach, PDT causes damage to lipid membranes through a series of photo-oxidation/peroxidation reactions induced by singlet oxygen.[13,14] The peroxidation reactions result in the cleavage of lipid chains[15] and hence can lead to changes in the structural characteristics of the lipids. Several studies have been dedicated to understanding these interactions of lipid membranes with different types of photosensitizers.[16−20] Particular attention has been paid to the interactions of MB with dioleoyl-*sn*-glycero-3-phosphocholine (DOPC) lipids. For example, Caetano et al. have reported structural damage and pore formation in giant unilamellar vesicles of DOPC as a function of the MB concentration.[21] Mertins et al. have studied the photodamage of DOPC and proposed models based on reaction-diffusion equations, supported by experimental data.[22] Schmidt et al. have shown that MB adsorbs to charged DOPC monolayers and changes the monolayer properties.[23] Yet, many questions still remain open on the molecular level regarding the structural and diffusion properties of lipid membranes. Molecular modeling, and in particular molecular dynamics simulations, provides an alternative route that can readily make the required information accessible. To date, several computational studies have been conducted on MB interactions with DNA at different scales.[24,25] However, to the best of our knowledge, only one modeling study is available on the MB−lipid interactions, which has investigated MB adsorption on a dimyristoylphosphatidic acid lipid monolayer through atomistic molecular dynamics simulations.[26]

Here, we investigate the MB and DOPC lipid bilayer interactions using a coarse-grained molecular model. Two different states, that is, neutral and cationic, of MB are considered. MB usually exists in a dissociated or oxidized state. Dissociated/oxidized MB is cationic and absorbs visible light strongly, emitting blue light.[27] On the other hand, the neutral MB can exist either as an undissociated salt or as a reduced MB (also called leucoMB), which is colorless (does not absorb light) and lipophilic.[28,29] As a couple, charged and neutral MB form a reversible oxidation−reduction system which has been employed in clinics to treat diseases[27] (e.g., in the treatment of methemoglobinemia, an NADPH methemoglobin reductase catalyzes the reduction of MB to leucoMB under physiological conditions to restore functional hemoglobin[30]). A coarse-grained model allows access to extended time and length scales which are needed for proper phase space sampling by omitting certain details of the molecular structure and decreasing the number of particles but retaining the general physics of the system. The MARTINI forcefield[31] is one such model where 2−4 heavy atoms are represented by a single bead. It has been extensively used to study lipid membranes,[31] proteins,[32] and

Received: February 2, 2018
Revised: March 11, 2018
Published: March 19, 2018

DOI: 10.1021/acs.langmuir.8b00372
Langmuir 2018, 34, 4314−4323

polymers.[33] Here, we develop a MARTINI model for MB based on atomistic reference simulations and use it in combination with existing MARTINI models for regular and peroxidized[34] DOPC lipids. We show that peroxidized lipids become more susceptible to both water and MB permeation compared to regular lipids.

COMPUTATIONAL METHODS

All molecular dynamics simulations were performed using the GROMACS software package[35] (version 5.0.4) in the NPT ensemble. Visual Molecular Dynamics (VMD)[36] was used for the visualization of the simulation evolution over time. Simulations were energy-minimized before the production runs using the steepest descent method. Other computational details are described below.

Simulations of MB. Partial charges for cationic and neutral states of MB were obtained from density functional theory (DFT) calculations via Gaussian 03[37] using the B3LYP functional and a basis set of 6-311+g(3d,3p). Chloride ion bonded to S or $N(CCH_3CH_3)$ atoms are considered for the undissociated salt forms of MB. Cationic MB was solvated in water, whereas neutral MB was solvated in heptane. (1-Octanol data was not available in Gaussian; therefore, heptane was selected to obtain the closest approximate values). The charges were calculated by CHELPG[38] (cf. Figures 1, S1, and Table S1 in Supporting Information).

For the atomistic simulations of MB, the OPLS-AA forcefield[39] with the TIP4P water model[40] was used with a time step of 2 ps. All bonds were constrained using LINCS.[41,42] The van der Waals cutoff was set to 1.0 nm, and Coulomb interactions were calculated using the particle-mesh Ewald method[43,44] with fourth order interpolation, 0.12 nm grid spacing, and 1.0 nm cut-off in real space. The Verlet cutoff scheme[45,46] with a cutoff distance of 1.0 nm was applied. Pressure and temperature were controlled by the Berendsen barostat[47] and the velocity rescale thermostat[48] with coupling times of 1.0 and 0.1 ps, respectively. Isotropic pressure coupling was used with a reference pressure of 1 bar and a compressibility of 4.5×10^{-5} bar^{-1}; temperature was set to 300 K. Production runs were performed for 70 ns with properties calculated by block averaging over the last 50 ns. Cationic and neutral states of MB were simulated in water (4012 molecules) and 1-octanol (369 molecules), respectively, and Cl^- was added to MB^+ in water simulations to neutralize the system charges.

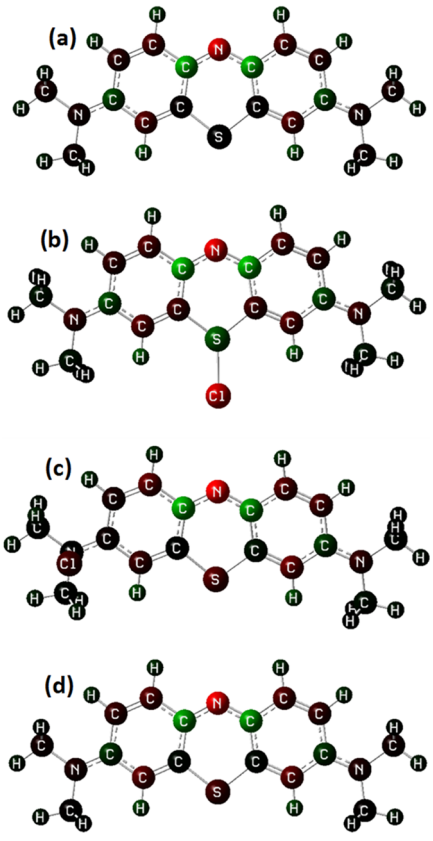

Figure 1. Distribution of partial charges for MB obtained from DFT calculations. (a) Cationic form is solvated in water. Undissociated form, where Cl is bonded to (b) S or (c) one of side N as well as the (d) neutral state of MB were solvated in heptane.

Free energies of solvation were calculated by thermodynamic integration in the NPT ensemble at 300 K and 1 bar, where the interaction of MB with water or 1-octanol was coupled to a parameter, λ, such that $\lambda = 0$ and $\lambda = 1$ indicated full and zero interactions, respectively, between the MB and solvent molecules. The temperature and pressure of these systems were controlled by the velocity rescale thermostat and the Parrinello–Rahman barostat.[49,50] In each solvent, 20 runs were performed for 40 ns, each corresponding to a different value of λ that was equally spaced. A soft core potential was used for nonbonded interactions with the parameters suggested by Shirts et al.[51,52] and Klimovich and Mobley[53] ($\alpha = 0.5$, soft-core power $p = 1$). The free energy of each constituent step was calculated using the multistate Bennett acceptance ratio,[51] and then ΔG_{ow} was obtained from the difference of ΔG in both solvents $[(\Delta G_{Ow}) = \Delta G_{MB^+ \text{ in water}} - \Delta G_{\text{neutral MB in octanol}}]$. The related thermodynamic cycle is given in Figure S2.

MARTINI Model for MB. The MARTINI model parameters for MB were optimized based on atomistic simulations. Eight beads were used to represent MB, and a combination of constraints, harmonic bonds, and harmonic improper dihedral potentials was used to keep the ring structure rigid. Standard MARTINI beads were used in the model. Model parameters are given in Table 1 and Figure 2. The same coarse-grained simulation parameters were used as in the MB/DOPC simulations below. Simulations were performed for 1.2 μs, and properties were obtained by block averaging over the last 1 μs. Bond and improper dihedral angle distributions derived from the atomistic simulations are shown in Figure 3. Free energy calculations were performed in water and 1-octanol for 1.2 μs to obtain the nonbonded interactions and the solvation energy data. The comparison of the free energy of transfer between 1-octanol and water obtained from experiments, all-atom simulations, and coarse-grained simulations is given in Tables 2 and S2.

Coarse-Grained Simulations of DOPC Double Bilayers. MARTINI force field was used to model regular and peroxidized double lipid bilayers. In the oxidized lipid MARTINI model, hydroperoxidation was assumed to act on the double bonds in lipid tails, resulting in a shift in the bonding position and addition of a side –OOH group; therefore, a polar MARTINI P2 bead is used instead of the nonpolar MARTINI C3 bead in regular DOPC. The bonding distance of P2 was kept at 0.33 nm, which is smaller than the regular bonding distance of 0.47 nm.[34] The difference in the structure of regular and peroxidized DOPC is provided in Figure S3, together with the assignments of MARTINI beads. The initial configurations of double bilayers for both lipid types were obtained by equally distributing 300 lipids over a grid in the upper and lower leaflets to form a symmetric bilayer, then the bilayer replicated by VMD TopoTools 1.6 plugin[61] such that the center-to-center distance between the bilayers of the same type is 11 nm. A total of 7114 MARTINI waters were randomly placed in the computational volume. Simulation parameters are the same as those used in coarse-grained simulations of the MB/DOPC system (see below). Simulations were performed for 1.2 μs and properties obtained by block averaging over the last 1 μs. Energy profiles were monitored to ensure equilibrium.

Coarse-Grained Simulations of the MB/DOPC System. MB molecules (150) were initially placed in the water layer between previously equilibrated two lipid bilayers (cf. Figure S4). To gain a better understanding on the transport of MB, one side of the membrane should be free of MB. Therefore, a double bilayer configuration was selected in the simulations. Each bilayer contained 300 lipids, with 150 lipids in each leaflet. The ratio of MB/lipid of 0.25

DOI: 10.1021/acs.langmuir.8b00372
Langmuir 2018, 34, 4314–4323

Table 1. MARTINI Model Parameters for MB^+ in Water and Neutral MB in 1-Octanol Corresponding to Dissociated and Undissociated Forms, Respectively[a]

		bead type (charge value) in 1-octanol	
bead number	bead type (charge value) in water MB^+	MB salt	neutral MB
1	SC_5 (0)	SC_5 (0)	SC_5 (0)
2	SC_5 (0)	SC_5 (0)	SC_5 (0)
3	SC_5 (0)	SQ_a (−0.500)	SC_5 (0)
4	SQ_0 (0.400)	SQ_d (0.500)	SN_a (0)
5	SC_5 (0)	SC_5 (0)	SC_5 (0)
6	SC_5 (0)	SC_5 (0)	SC_5 (0)
7	SQ_0 (0.300)	SN_a (0)	SN_a (0)
8	SQ_0 (0.300)	SN_a (0)	SN_a (0)
		bonds	
i j	bonds length (nm) / K_{bond} (kJ mol^{-1} nm^{-2})	bonds length (nm) / K_{bond} (kJ mol^{-1} nm^{-2})	bonds length (nm) / K_{bond} (kJ mol^{-1} nm^{-2})
1 2	0.221 constraint	0.221 constraint	0.221 constraint
2 7	0.233 constraint	0.234 constraint	0.232 constraint
1 4	0.306 constraint	0.306 constraint	0.306 constraint
2 3	0.302 constraint	0.304 constraint	0.302 constraint
3 4	0.186 constraint	0.248 constraint	0.188 constraint
4 5	0.306 constraint	0.306 constraint	0.306 constraint
3 6	0.302 constraint	0.304 constraint	0.302 constraint
5 6	0.221 constraint	0.221 constraint	0.221 constraint
6 8	0.233 constraint	0.234 constraint	0.232 constraint
4 6	0.363 75 000	0.363 75 000	0.365
3 5	0.367 75 000	0.404 75 000	0.367
1 3	0.367 75 000	0.404 75 000	0.367
2 4	0.363 75 000	0.363 75 000	0.363
		impropers	
i j k l	angle (deg) / $K_{improper}$ (kJ mol^{-1} rad^{-2})	angle (deg) / $K_{improper}$ (kJ mol^{-1} rad^{-2})	angle (deg) / $K_{improper}$ (kJ mol^{-1} rad^{-2})
4 1 2 5	0.0 270.0	0.0 270.0	0.0
3 2 4 6	0.0 270.0	0.0 270.0	0.0
1 2 3 4	0.0 270.0	0.0 270.0	0.0
5 6 3 4	0.0 270.0	0.0 270.0	0.0
2 1 4 3	0.0 270.0	0.0 270.0	0.0
6 5 4 3	0.0 270.0	0.0 270.0	0.0

[a]Bead types are as defined in the MARTINI model,[31] but the charges are updated based on DFT calculation.

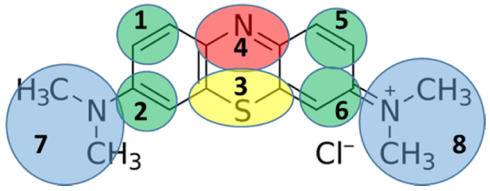

Figure 2. MARTINI mapping scheme for each bead number.

was selected such that it is in the range where DOPC disruption has been reported.[21] Cl^- ions (150) neutralize the charge. A total number of 7114 MARTINI waters were in the system, ensuring full hydration with a hydration level of 47 waters/lipid. Regular and oxidized MARTINI models were used for lipids, together with our MARTINI model for MB. The distance between the equilibrated bilayers covering the region where MB was initially located was 4.1 ± 0.2 and 3.8 ± 0.3 nm, respectively, for regular and peroxidized lipids. These values were determined based on the phosphate head (P−P) distance calculations. Simulations were conducted in an NPT ensemble with a time step of 20 fs. The neighbor list was updated every 10 steps. Pressure and temperature were maintained at 1 bar and 300 K using the Berendsen barostat and the velocity rescale thermostat, respectively. Lipid, water (including Cl^-), and MB temperatures were coupled separately with a coupling time of 1.0 ps, the pressure of the system was controlled by semi-isotropic volume scaling (separately in and out of the bilayer plane) with a coupling time of 2.0 ps and a compressibility factor of 1 × 10^{-5} bar^{-1}. Electrostatic interactions were treated using a Reaction field zero scheme with a potential shift modifier.[62,63] Van der Waals interactions were treated with a shifted potential cutoff scheme. The cutoff radii for van der Waals and electrostatic interactions were 1.2 nm. The Lennard-Jones and Coulomb potentials were smoothly

Table 2. Model Versus Experimental Free Energy of Transfer between Water and 1-Octanol for MB

		ΔG_{ow} (kJ/mol)
experimental[54−60]		−4.54 to +10.83
all-atom simulations	between MB^+ in water and undissociated MB salt with Cl bonded to S in 1-octanol (ΔG_{Ow}) = $\Delta G_{MB^+ \text{ in water}} - \Delta G_{\text{neutral MB in octanol}}$	5.5
	between MB^+ in water and undissociated MB salt with Cl bonded to side N in 1-octanol (ΔG_{Ow}) = $\Delta G_{MB^+ \text{ in water}} - \Delta G_{\text{neutral MB salt in octanol}}$	9.8
	between MB^+ in water and neutral MB (ΔG_{Ow}) = $\Delta G_{MB^+ \text{ in water}} - \Delta G_{\text{neutral MB in octanol}}$	20.6
	between MB^+ in water and 1-octanol (ΔG_{OwMB^+}) = $\Delta G_{MB^+ \text{ in water}} - \Delta G_{MB^+ \text{ in octanol}}$	−67.1
coarse-grained simulations	between MB^+ in water and undissociated MB salt in 1-octanol (ΔG_{Ow}) = $\Delta G_{MB^+ \text{ in water}} - \Delta G_{\text{neutral MB salt in octanol}}$	7.8
	between MB^+ in water and neutral MB in 1-octanol (ΔG_{Ow}) = $\Delta G_{MB^+ \text{ in water}} - \Delta G_{\text{neutral MB in octanol}}$	22.4

DOI: 10.1021/acs.langmuir.8b00372
Langmuir 2018, 34, 4314−4323

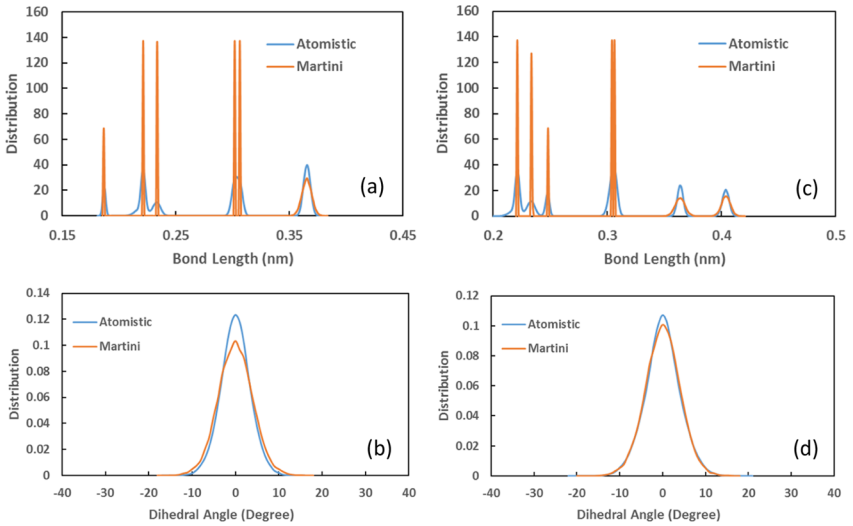

Figure 3. Bond (top) and improper dihedral angle (bottom) distributions of cationic (left) and neutral (right) forms of MB obtained from the all-atom and coarse-grained simulations.

Table 3. Average Properties of Regular and Peroxidized MARTINI DOPC Double Lipid Bilayers

	membrane thickness (nm)	area per lipid head group (nm^2)	lateral diffusion coefficient ($\mu m^2/s$)
regular DOPC	4.48 ± 0.02	0.65 ± 0.03	31.9 ± 7.5 @ 300 K
peroxidized DOPC	4.04 ± 0.06	0.77 ± 0.01	26.7 ± 5.8 @ 300 K
experimental findings for regular DOPC	3.53−4.6[67−72]	0.67−0.73[67−71,73]	9.32 @ 298 K,[74] 11.5 @ 303 K[74]

shifted to zero between 0.9 and 1.2 nm and between 0.0 and 1.2 nm, respectively. Systems were simulated for 5 μs, and the properties were evaluated by block averaging the trajectories. Total energy of the systems throughout the simulations indicating the simulation have reached the equilibrium is given Figure S5.

RESULTS AND DISCUSSION

Partitioning Free Energies of MB between Water and 1-Octanol. MB is soluble in water but only slightly soluble in alcohol.[64,65] It forms an electron donor−acceptor pair together with its neutral state that has the potential to undergo reversible oxidation−reduction reactions in the presence of molecular oxygen[66] because of the thiazine ring and imine groups. In its reduced state, the cationic dye is uncharged and lipophilic, and it can be re-oxidized within the cell after crossing the plasma membrane by diffusion.[29] Hence, we focus on two states of MB: the cationic MB^+ and the neutral MB. Because MB is slightly soluble in alcohol, we assume that the salt exists mostly in its undissociated neutral form in oily alcohols. Therefore, for the neutral MB, 3 different forms have been considered: (1) reduced MB (with no Cl^- ions bound), (2) undissociated MB salt where Cl^- is bonded to one of the side N, and (3) undissociated MB salt where Cl^- is bonded to the central S. For both atomistic and coarse-grained simulations, free energies of solvation have been computed in water for MB^+ and in 1-octanol for neutral MB. The reason for selecting water and octanol as solvents is that experimental partition coefficients for MB were mostly obtained by dissolving MB in water and octanol.[54−58] Only for MB^+ in the atomistic case did we compute the free energy of solvation in both water and 1-octanol for comparison of the data with the reported atomistic modeling results.[26] Free energies of transfer between water and 1-octanol (ΔG_{Ow}) were obtained by subtracting the free energy of solvation of neutral MB in 1-octanol from the free energy of solvation of MB^+ in water [$(\Delta G_{Ow}) = \Delta G_{MB^+ \text{ in water}} - \Delta G_{\text{neutral MB in octanol}}$]. For the atomistic MB^+ case, the free energy of solvation of MB^+ in 1-octanol was subtracted from the free energy of solvation of MB^+ in water [$(\Delta G_{OwMB^+}) = \Delta G_{MB^+ \text{ in water}} - \Delta G_{MB^+ \text{ in octanol}}$]. Results are given in Table 2. For the atomistic simulations, ΔG_{Ow} values are found to be 5.5, 9.8, and 20.6 kJ/mol for MB salts where Cl^- is bonded to S or N atoms, together with reduced MB. The values for undissociated salt are in agreement with experiments that show variations between −4.54 and +10.83 kJ/mol.[54−58,60] Experimentally, the different bonding positions are not

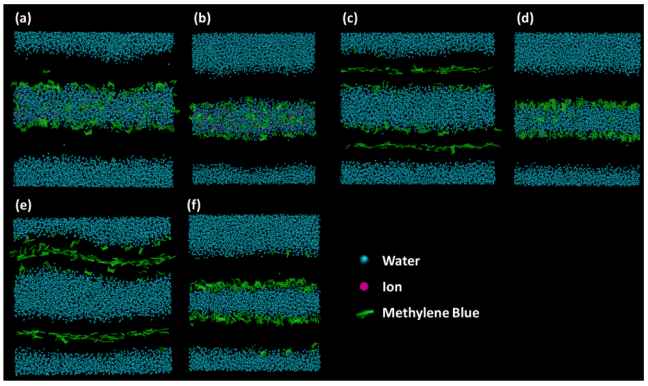

Figure 4. Final configurations of MB distributions with respect to lipid bilayers systems: (a) MB^+—peroxidized DOPC, (b) MB^+—regular DOPC, (c) MB salt—peroxidized DOPC, (d) MB salt—regular DOPC, (e) reduced MB—peroxidized DOPC, and (f) reduced MB—regular DOPC. For simplicity, lipid bilayers are not shown in (a−f), and Cl^- is represented by magenta beads in (a,b). MB^+ mostly accumulates at the surface but may cross the peroxidized DOPC bilayers (a). Both forms of neutral MB (MB salt and reduced MB) tend to accumulate in the center of peroxidized bilayers (c,e). No transport of MB across regular DOPC is observed (b,d) except for the reduced form of MB (f).

DOI: 10.1021/acs.langmuir.8b00372
Langmuir 2018, 34, 4314−4323

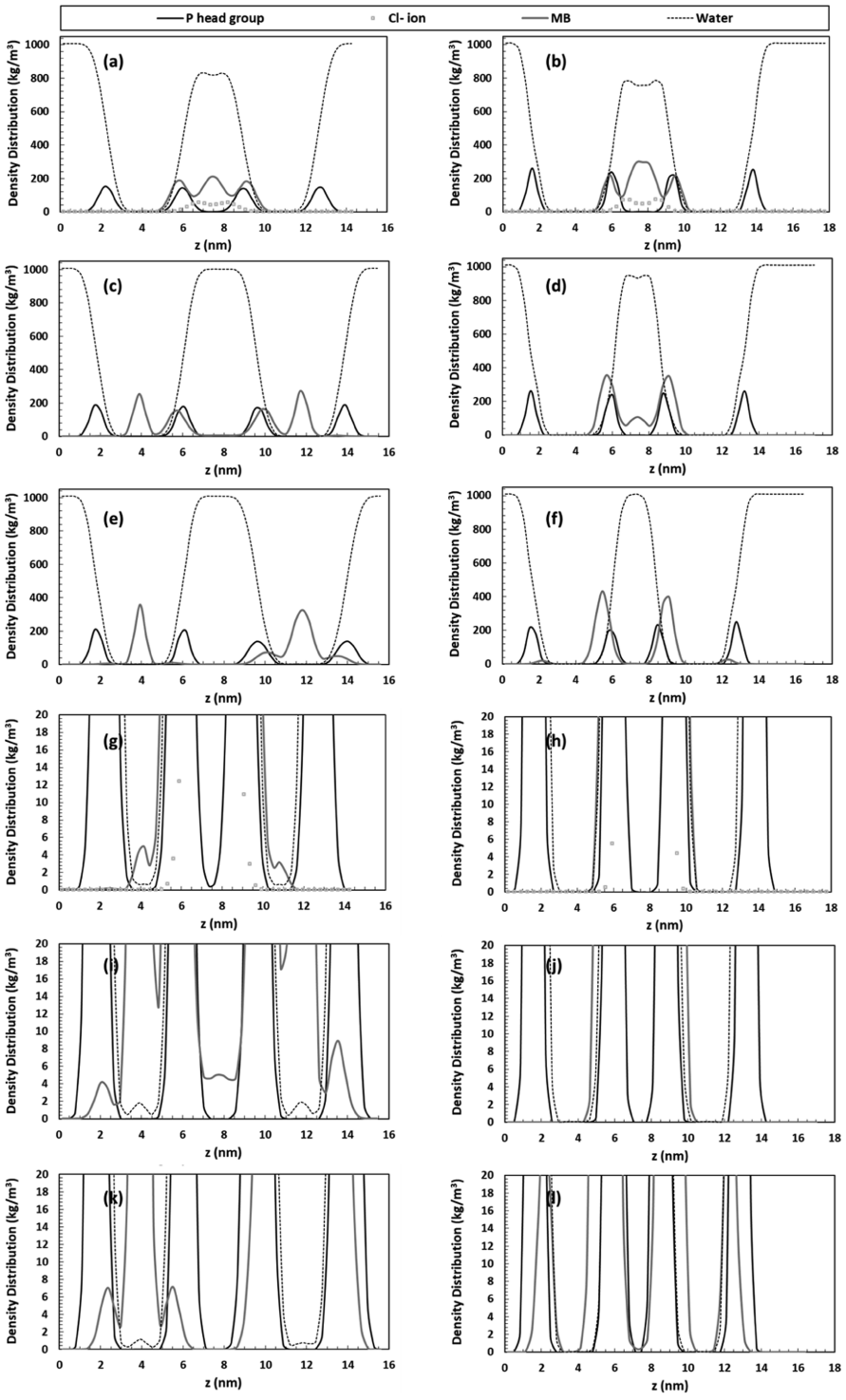

Figure 5. Density distribution of MB, water, Cl^- with respect to phosphate head groups for systems containing (a) MB^+—peroxidized DOPC, (b) MB^+—regular DOPC, (c) MB salt—peroxidized DOPC, (d) MB salt—regular DOPC, (e) reduced MB—peroxidized DOPC, and (g) reduced MB—regular DOPC. Enlarged images of (a–f) are given in (g–l), respectively. MB facilitates water transport especially through peroxidized lipid bilayers. All forms of MB cross the bilayer in the presence of peroxidized lipids.

distinguished. Because MB dye exists in the form of salt, this form is used in the experiments to obtain the partition coefficients. However, for reduced MB, a higher transfer free energy value is obtained, and to our knowledge, no study has reported the partition coefficient for leucoMB yet. Moreover, ΔG_{OwMB^+} of MB^+ is computed as −67.1 kJ/mol, which is in good agreement with the previously computed value of −66.6 kJ/mol.[26] These findings support our assumption that MB^+ mostly exists in its undissociated state in oily alcohols. With the MARTINI coarse-grained model, on the other hand, the best ΔG_{Ow} value using the undissociated salt for the neutral state of MB is found to be 7.8 kJ/mol, which is in between the computed values of atomistic simulations, that is, 5.5 and 9.8 kJ/mol. The MARTINI model cannot capture the difference

DOI: 10.1021/acs.langmuir.8b00372
Langmuir 2018, 34, 4314−4323

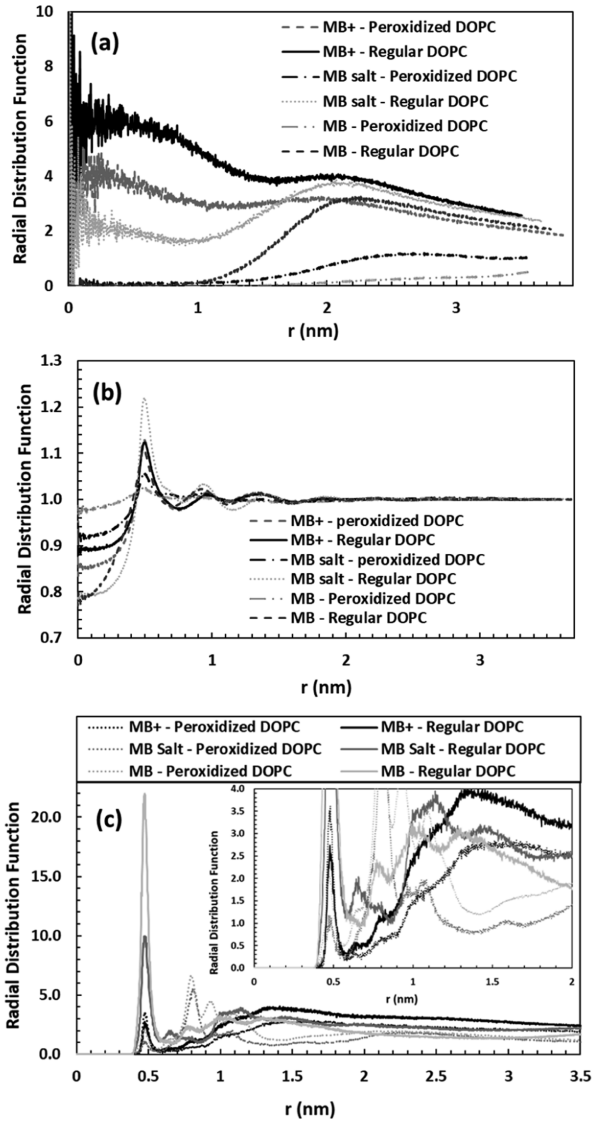

Figure 6. Center of mass (a) and lateral (b) radial distribution functions (RDFs) of MB with respect to the P head group of the bilayers. MB^+ tends to accumulate at the water/lipid interface of the bilayers, and neutral MB aggregates inside the bilayer of peroxidized lipids and at the water/lipid interface of regular lipids. In 2D, nearly uniform distribution of neutral MB is observed with peroxidized lipids, while distinct short range ordering is evident with regular lipids. (c) Spatial intermolecular RDF of MB with respect to MB. MB in peroxidized lipids is shown by dotted lines. The enlarged image is given in the inset for a better representation. In regular DOPC, a clear short-range ordering is obtained with neutral MB, which is followed by MB salt and MB. In peroxidized lipids, neutral forms of MB are more ordered than MB^+.

between the two undissociated forms of MB. Therefore, only one model is used for the undissociated form of MB for further calculations. The ΔG_{Ow} value using the MARTINI model of reduced MB (leucoMB), however, is 22.4 kJ/mol, which is within the accepted range of variation. Altogether, coarse-grained and atomistic data are in good agreement with experimental data.

Structural Properties of Regular and Peroxidized DOPC Bilayers. Structural properties of both regular and peroxidized DOPC double bilayers in the absence of MB are computed at 300 K and compared with literature values (cf. Table 3). With the standard MARTINI DOPC lipid bilayer model, we calculate 4.48 ± 0.02 nm of membrane thickness based on the distance between phosphate head groups and 0.65 ± 0.03 nm^2 of area per lipid head group values, both of which are in good agreement with experiments.[67−73] However, a higher diffusivity is obtained compared to the experiments,[74] which is not surprising as coarse-graining often predicts up to 10× faster diffusion.[34] A higher area per lipid and lower membrane thickness were obtained with the peroxidized lipid model. The increase in the area per lipid head group and decrease in thickness are 18.5 and 9.8%, respectively, which are similar to the values of 19.5 and 8.1% reported for oxidized lipids.[34,75] This change was mainly attributed to the changes in chemical affinity and polarity because of the addition of hydroperoxide groups.[34] However, although lower diffusivity values were obtained with peroxidized lipids, the decrease is only 16% compared to the 29% of a previously computed value.[34]

Structural Properties of DOPC Bilayers in the Presence of MB. Interactions of MB with the DOPC bilayers are studied considering six cases: (a) peroxidized DOPC bilayers in the presence of MB^+, (b) regular DOPC bilayers in the presence of neutral MB^+, (c) peroxidized DOPC lipid bilayers in the presence of the undissociated MB salt, (d) regular lipid bilayers in the presence of the undissociated MB salt, (e) peroxidized lipid bilayers in the presence of reduced MB, and (f) regular lipid bilayers in the presence of reduced MB. Final simulation configurations and the density distribution profiles of MB, DOPC (phosphate in the head group) and Cl^- corresponding to each system are given in Figures 4 and 5, respectively. With peroxidized DOPC lipid bilayers, the diffusion of both MB^+ and neutral MB, together with water is observed across the lipid bilayer (Figure 4a,c,e, 5a,c,e,g,i,k). While neutral MB tends to gather in the center of the peroxidized bilayer, MB^+ mostly accumulates at the bilayer surface because of the charge penalty in the apolar center; its concentration throughout the bilayer gradually decreases. On the other hand, for the regular DOPC lipid bilayer, no diffusion of water or either state of MB (expect for reduced MB) is observed across the bilayer (Figures 4b,d, 5b,d,h,j). Only reduced MB is observed to transport across the bilayer and accumulate on both surfaces of the regular bilayer (Figure 4f, 5f,l). While MB^+ stays mostly in the water phase between the bilayers, both undissociated MB salt and reduced MB accumulates slightly below the hydrophilic head groups of regular DOPC. A slight depletion in water density is observed at the points where MB^+ or MB salt are concentrated between the bilayers because of the amphipathic and self-associative nature of the molecule.

To obtain a better understanding on the molecular ordering of MB^+, MB salt, and reduced MB, the center of mass (com) and spatial RDFs are computed (cf. Figure 6). In agreement with the previous findings, com-RDFs with respect to the P in the head group of bilayers (Figure 6a) reveal that MB^+ accumulates in the water phase between the bilayers or at the water/lipid interface and reduced MB aggregates inside both lipid bilayers. We clearly see a broad maximum at very low distances and a weaker maximum at about 2 nm with a weak intervening minimum. For undissociated MB salt, however, both conditions are observed; that is, MB salt accumulates inside the peroxidized lipid bilayers and aggregates at the water/lipid interface and the water phase of regular lipid bilayers. In addition, spatial RDF calculations with respect to

DOI: 10.1021/acs.langmuir.8b00372
Langmuir 2018, 34, 4314−4323

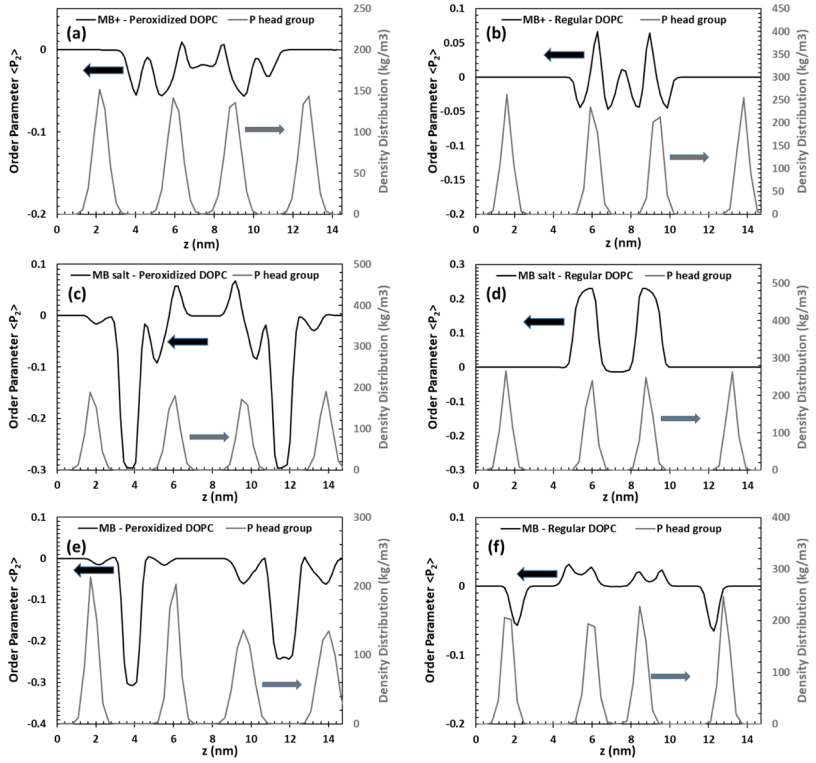

Figure 7. Order parameter $\langle P_2 \rangle$ of MB along the direction of the membrane normal for (a) MB^+—peroxidized DOPC, (b) MB^+—regular DOPC, (c) MB salt—peroxidized DOPC, (d) MB salt—regular DOPC, (e) reduced MB—peroxidized DOPC, and (f) reduced MB—regular DOPC. Density distribution of P head groups is included for each case for a better comparison. MB^+ is more randomly distributed across the bilayer compared to MB salt and reduced MB. MB salt makes 68° and 46° with the membrane normal, respectively, at the center of the bilayer with peroxidized DOPC and at the bilayer/water interface with regular DOPC. Reduced MB makes 57° with the membrane normal at the bilayer/water interface with regular DOPC and 69° and 65° with the membrane normal at the center of the peroxidized bilayers.

Table 4. Average Properties of Regular and Peroxidized MARTINI DOPC Double Lipid Bilayers in the Presence of MB^+ and Neutral MB

		membrane thickness (nm)	area per lipid head group (nm^2)	lateral diffusion coefficient of P @ 300 K ($\mu m^2/s$)	lateral/z-direction diffusion coefficient of MB @ 300 K ($\mu m^2/s$)
regular DOPC	MB^+	4.42 ± 0.02	0.675 ± 0.4 × 10^{-2}	29.3 ± 0.6	78.2 ± 1.6
	MB salt	4.34 ± 0.02	0.698 ± 0.4 × 10^{-2}	29.5 ± 9.8	50.9 ± 2.6
	MB	4.28 ± 0.02	0.723 ± 0.2 × 10^{-2}	24.4 ± 0.3	21.4 ± 5.6/0.2 ± 0.6 × 10^{-2}
peroxidized DOPC	MB^+	3.77 ± 0.04	0.857 ± 0.5 × 10^{-2}	14.9 ± 0.6	68.7 ± 16.8
	MB salt	4.18 ± 0.07	0.792 ± 0.5 × 10^{-2}	45.9 ± 13.0	39.0 ± 10.5/0.5 ± 0.3 × 10^{-1}
	MB	4.25 ± 0.06	0.784 ± 0.4 × 10^{-2}	23.0 ± 17.5	30.8 ± 23.9/0.2 ± 0.3 × 10^{-1}

head group P (Figure 6b) show that reduced MB has a strong affinity to peroxidized lipid head groups, and MB salt has a weak affinity to regular lipid head groups at short distances. A nearly random distribution of reduced MB is obtained in peroxidized bilayers, and a more ordered conformation of MB salt is observed in regular bilayers. For either form of neutral MB, higher affinity for peroxidized lipids is observed compared to regular lipids. However, the opposite behavior is observed for MB^+. Intermolecular RDFs between MBs have also been computed (Figure 6c). An extremely sharp (crystalline) peak and hence a very high short-range ordering are obtained with reduced MB in regular DOPC, which is followed by MB salt in regular DOPC. In peroxidized lipids, distinct second and third peaks indicate that long-range ordering exists and is more probable than very short ordering in the presence of reduced MB and neutral MB salt. For MB^+, short-range ordering is more significant in peroxidized lipids than the regular lipids.

To characterize the orientation of MB, order parameters are calculated along the z axis using the relation $\langle P_2 \rangle = \left\langle \frac{3\cos 2\theta - 1}{2} \right\rangle$ where θ is the angle formed by the long axis of MB with the bilayer normal (Figure 7). $\langle P_2 \rangle$ of −0.5 and 1 indicate perfect perpendicular and parallel orientations of MB with respect to the z axis, respectively, whereas a value of 0 represents a random orientational distribution of MB. MB^+ in general has a random orientation throughout both lipid bilayers, except for at the center of the peroxidized bilayer where it aligns on average at ∼60° with the bilayer normal. Similarly, MB salt prefers a mostly parallel orientation at the center of peroxidized DOPC (orientation angle of ∼68°). On the other hand, MB salt aligns at ∼47° with the z axis, at the bilayer/water interface, that is, the phosphate groups, in regular

DOI: 10.1021/acs.langmuir.8b00372
Langmuir 2018, 34, 4314−4323

DOPC. Between the double bilayers, MB salt has a random orientation in all cases. Reduced MB has a similar orientation in peroxidized DOPC bilayers but a more random distribution in regular DOPC. These findings agree well with previous reports.[26]

Structural and dynamic properties of the double bilayers in the presence of MB are monitored by calculating the average thickness, the area per lipid head group, the lateral diffusion coefficient of the bilayers as well as the diffusion coefficient of MB (both lateral and along the bilayer normal). Diffusion coefficients were calculated from linear fits of mean square displacement curves of lipid/MB centers of masses with respect to time (Table 4). A thinning effect is observed in regular DOPC bilayers in the presence of MB. The thinning is most significant in the presence of reduced MB and least significant with MB^+. In preoxidized lipids, however, although a thinning is observed with MB^+, both neutral forms of MB have resulted in an increase in the membrane thickness. This is attributed to the incorporation of MB at the center of the bilayers. All forms of MB have in general resulted in an increase in the area per lipid; the most significant increase for peroxidized DOPC in the presence of MB^+ and for regular DOPC in the presence of reduced MB are both ∼11%. Within the error bound, no significant change in the lateral diffusion coefficient of the bilayer is detected for regular DOPC. For peroxidized lipids, ∼44% decrease in the lateral diffusion coefficient is observed with MB^+, which is a result of stronger lipid/MB interactions. The presence of undissociated MB salt in peroxidized lipids, on the other hand, fluidizes the membrane, causing ∼72% increase in the lateral diffusion coefficient of the bilayer. No significant difference in lateral diffusion coefficient is observed for reduced MB in peroxidized lipids. Regarding the lateral diffusion of MB, MB^+ has the highest diffusivities flowed by undissociated MB salt and reduced MB. For all forms of MB, no significant changes in the lateral diffusivities are observed in either regular or peroxidized lipids. For diffusion of MB along z direction, however, diffusivities of 0.2 ± 0.006, 0.5 ± 0.03, and 0.2 ± 0.03 $\mu m^2/s$ are obtained across regular DOPC bilayers in the presence of reduced MB and across peroxidized bilayers in the presence of undissociated MB salt and reduced MB, respectively. No transport can be recorded for all other cases.

CONCLUSIONS

We present a coarse-grained MARTINI model for MB and investigate its interaction with regular and peroxidized DOPC lipid bilayers. Partial charges for MB were obtained through DFT calculations for use with the OPLS-AA force field, and MARTINI parameters were optimized based on these atomistic simulations. Free energy calculations suggest that MB remains in the undissociated (neutral) form in the oil phase. Cationic and neutral (undissociated salt and reduced) states of MB were incorporated separately to regular or peroxidized double bilayers systems, and their effect on membrane disruption was monitored. All forms of MB can diffuse across the peroxidized bilayers, although they accumulate at one of the bilayer surfaces with regular DOPC bilayers except for the reduced MB where MB is observed to sit on both surfaces of the bilayers. With peroxidized bilayers, neutral MB (both reduced and undissociated salt) mostly gather at the center of the bilayer and drag water molecules along to the center. However, the density of cationic MB decreases gradually across the peroxidized bilayer. The most significant changes in the membrane properties were obtained in this case of peroxidized DOPC bilayer in the presence of MB^+, with an increase of ∼11% in the membrane area and a decrease of ∼44% in lateral diffusivity of the bilayer. Our results indicate that the charge state of MB and the oxidation degree of the DOPC lipid bilayer play an important role in membrane properties and hence provide a key to understanding photoinduced biomembrane damage.

ASSOCIATED CONTENT

Supporting Information

The Supporting Information is available free of charge on the ACS Publications website at DOI: 10.1021/acs.langmuir.8b00372.

Distributions of partial charge determined by DFT, thermodynamic cycle to determine ΔG, description of peroxidation reaction, MARTINI representation of regular and peroxidized DOPC, visualization of initial simulation configurations, energy profiles showing equilibration, and table of charges (PDF)

AUTHOR INFORMATION

Corresponding Author

*E-mail: rfaller@ucdavis.edu.

ORCID

Roland Faller: 0000-0001-9946-3846

Notes

The authors declare no competing financial interest.

ACKNOWLEDGMENTS

This work was supported by a grant from the University of California Office of the President UCOP Lab Fee Program (grant number 12-LR-237353) and was partially performed under the auspices of the U. S. Department of Energy by Lawrence Livermore National Laboratory (LLNL) under contract DE-AC52-07NA27344. Computations were partially performed at LLNL Aztec and Sierra massively parallel computers. Analysis was partially performed at TUBITAK ULAKBIM, High Performance and Grid Computing Center (TRUBA resources).

REFERENCES

(1) Sami, M.; Ikeda, M.; Yabuuchi, S. Evaluation of the alkaline methylene blue staining method for yeast activity determination. *J. Ferment. Bioeng.* **1994**, *78*, 212−216.

(2) Ginimuge, P. R.; Jyothi, S. D. Methylene blue: revisited. *J. Anaesthesiol., Clin. Pharmacol.* **2010**, *26*, 517.

(3) Orth, K.; Beck, G.; Genze, F.; Rück, A. Methylene blue mediated photodynamic therapy in experimental colorectal tumors in mice. *J. Photochem. Photobiol., B* **2000**, *57*, 186−192.

(4) Lim, E. J.; Oak, C.-H.; Heo, J.; Kim, Y.-H. Methylene blue-mediated photodynamic therapy enhances apoptosis in lung cancer cells. *Oncol. Rep.* **2013**, *30*, 856−862.

(5) Samy, N. A.; Salah, M. M.; Ali, M. F.; Sadek, A. M. Effect of methylene blue-mediated photodynamic therapy for treatment of basal cell carcinoma. *Laser Med. Sci.* **2015**, *30*, 109−115.

(6) Khanal, A.; Bui, M.-P. N.; Seo, S. S. Microgel-encapsulated methylene blue for the treatment of breast cancer cells by photodynamic therapy. *J. Breast Cancer* **2014**, *17*, 18−24.

(7) Wainwright, M.; Crossley, K. B. Methylene Blue-a therapeutic dye for all seasons? *J. Chemother.* **2013**, *14*, 431−443.

(8) Sperandio, F.; Huang, Y.-Y.; Hamblin, M. Antimicrobial photodynamic therapy to kill Gram-negative bacteria. *Recent Pat. Anti-Infect. Drug Discovery* **2013**, *8*, 108−120.

DOI: 10.1021/acs.langmuir.8b00372
Langmuir 2018, 34, 4314−4323

(9) Alvarenga, L. H.; Prates, R. A.; Yoshimura, T. M.; Kato, I. T.; Suzuki, L. C.; Ribeiro, M. S.; Ferreira, L. R.; dos Santos Pereira, S. A.; Martinez, E. F.; Saba-Chujfi, E. Aggregatibacter actinomycetemcomitans biofilm can be inactivated by methylene blue-mediated photodynamic therapy. *Photodiagn. Photodyn. Ther.* **2015**, *12*, 131−135.
(10) Redmond, R. W.; Gamlin, J. N. A compilation of singlet oxygen yields from biologically relevant molecules. *Photochem. Photobiol.* **1999**, *70*, 391−475.
(11) Gabrielli, D.; Belisle, E.; Severino, D.; Kowaltowski, A. J.; Baptista, M. S. Binding, aggregation and photochemical properties of methylene blue in mitochondrial suspensions. *Photochem. Photobiol.* **2004**, *79*, 227−232.
(12) Chen, Y.; Zheng, W.; Li, Y.; Zhong, J.; Ji, J.; Shen, P. Apoptosis induced by methylene-blue-mediated photodynamic therapy in melanomas and the involvement of mitochondrial dysfunction revealed by proteomics. *Cancer Sci.* **2008**, *99*, 2019−2027.
(13) Thorpe, W. P.; Toner, M.; Ezzell, R. M.; Tompkins, R. G.; Yarmush, M. L. Dynamics of photoinduced cell plasma membrane injury. *Biophys. J.* **1995**, *68*, 2198.
(14) Mitsunaga, M.; Ogawa, M.; Kosaka, N.; Rosenblum, L. T.; Choyke, P. L.; Kobayashi, H. Cancer cell-selective in vivo near infrared photoimmunotherapy targeting specific membrane molecules. *Nat. Med.* **2011**, *17*, 1685−1691.
(15) Gollnick, K. Type II Photooxygenation Reactions in Solution. *Advances in Photochemistry*; John Wiley & Sons, Inc., 2007; Vol *6*, pp 1−122.
(16) Lavi, A.; Weitman, H.; Holmes, R. T.; Smith, K. M.; Ehrenberg, B. The depth of porphyrin in a membrane and the membrane's physical properties affect the photosensitizing efficiency. *Biophys. J.* **2002**, *82*, 2101−2110.
(17) Pashkovskaya, A.; Kotova, E.; Zorlu, Y.; Dumoulin, F.; Ahsen, V.; Agapov, I.; Antonenko, Y. Light-triggered liposomal release: membrane permeabilization by photodynamic action. *Langmuir* **2010**, *26*, 5726−5733.
(18) Sholto, A.; Ehrenberg, B. Hydrophobicity, topography in membranes and photosensitization of silicon phthalocyanines with axial ligands of varying lengths. *Photochem. Photobiol. Sci.* **2008**, *7*, 344−351.
(19) Cordeiro, R. M.; Miotto, R.; Baptista, M. S. Photodynamic efficiency of cationic meso-porphyrins at lipid bilayers: insights from molecular dynamics simulations. *J. Phys. Chem. B* **2012**, *116*, 14618−14627.
(20) Santos, A.; Rodrigues, A. M.; Sobral, A. J. F. N.; Monsanto, P. V.; Vaz, W. L. C.; Moreno, M. J. Early Events in Photodynamic Therapy: Chemical and Physical Changes in a POPC: Cholesterol Bilayer due to Hematoporphyrin IX-mediated Photosensitization. *Photochem. Photobiol.* **2009**, *85*, 1409−1417.
(21) Caetano, W.; Haddad, P. S.; Itri, R.; Severino, D.; Vieira, V. C.; Baptista, M. S.; Schröder, A. P.; Marques, C. M. Photo-induced destruction of giant vesicles in methylene blue solutions. *Langmuir* **2007**, *23*, 1307−1314.
(22) Mertins, O.; Bacellar, I. O. L.; Thalmann, F.; Marques, C. M.; Baptista, M. S.; Itri, R. Physical damage on giant vesicles membrane as a result of methylene blue photoirradiation. *Biophys. J.* **2014**, *106*, 162−171.
(23) Schmidt, T. F.; Caseli, L.; Oliveira, O. N., Jr.; Itri, R. Binding of Methylene Blue onto Langmuir Monolayers Representing Cell Membranes May Explain Its Efficiency as Photosensitizer in Photodynamic Therapy. *Langmuir* **2015**, *31*, 4205−4212.
(24) Nogueira, J. J.; González, L. Molecular dynamics simulations of binding modes between methylene blue and DNA with alternating GC and AT sequences. *Biochemistry* **2014**, *53*, 2391−2412.
(25) Rohs, R.; Sklenar, H.; Lavery, R.; Röder, B. Methylene blue binding to DNA with alternating GC base sequence: a modeling study. *J. Am. Chem. Soc.* **2000**, *122*, 2860−2866.
(26) Casares, J. J. G.; Camacho, L.; Martín-Romero, M. T.; Cascales, J. J. L. Methylene blue adsorption on a DMPA lipid Langmuir monolayer. *ChemPhysChem* **2010**, *11*, 2241−2247.
(27) Oz, M.; Lorke, D. E.; Hasan, M.; Petroianu, G. A. Cellular and Molecular Actions of Methylene Blue in the Nervous System. *Med. Res. Rev.* **2011**, *31*, 93−117.
(28) Lee, S.-K.; Mills, A. Novel photochemistry of leuco-Methylene Blue. *Chem. Commun.* **2003**, *18*, 2366−2367.
(29) May, J. M.; Qu, Z.-C.; Whitesell, R. R. Generation of oxidant stress in cultured endothelial cells by methylene blue: protective effects of glucose and ascorbic acid. *Biochem. Pharmacol.* **2003**, *66*, 777−784.
(30) Bradberry, S. M. Occupational methaemoglobinaemia. *Toxicol. Rev.* **2003**, *22*, 13−27.
(31) Marrink, S. J.; Risselada, H. J.; Yefimov, S.; Tieleman, D. P.; de Vries, A. H. The MARTINI force field: coarse grained model for biomolecular simulations. *J. Phys. Chem. B* **2007**, *111*, 7812−7824.
(32) Monticelli, L.; Kandasamy, S. K.; Periole, X.; Larson, R. G.; Tieleman, D. P.; Marrink, S.-J. The MARTINI coarse-grained force field: extension to proteins. *J. Chem. Theory Comput.* **2008**, *4*, 819−834.
(33) Lee, H.; de Vries, A. H.; Marrink, S.-J.; Pastor, R. W. A coarse-grained model for polyethylene oxide and polyethylene glycol: conformation and hydrodynamics. *J. Phys. Chem. B* **2009**, *113*, 13186−13194.
(34) Guo, Y.; Baulin, V. A.; Thalmann, F. Peroxidised phospholipid bilayers: insight from coarse-grained molecular dynamics simulations. *Soft Matter* **2016**, *12*, 263−271.
(35) Berendsen, H. J. C.; van der Spoel, D.; van Drunen, R. GROMACS: A message-passing parallel molecular dynamics implementation. *Comput. Phys. Commun.* **1995**, *91*, 43−56.
(36) Humphrey, W.; Dalke, A.; Schulten, K. VMD: visual molecular dynamics. *J. Mol. Graphics* **1996**, *14*, 33−38.
(37) Frisch, M. J.; Trucks, G. W.; Schlegel, H. B.; Scuseria, G. E.; Robb, M. A.; Cheeseman, J. R.; Scalmani, G.; Barone, V.; Mennucci, B.; Petersson, G. A.; Nakatsuji, H.; Caricato, M.; Li, X.; Hratchian, H. P.; Izmaylov, A. F.; Bloino, J.; Zheng, G.; Sonnenberg, J. L.; Hada, M.; Ehara, M.; Toyota, K.; Fukuda, R.; Hasegawa, J.; Ishida, M.; Nakajima, T.; Honda, Y.; Kitao, O.; Nakai, H.; Vreven, T.; Montgomery, J. A., Jr.; Peralta, J. E.; Ogliaro, F.; Bearpark, M. J.; Heyd, J.; Brothers, E. N.; Kudin, K. N.; Staroverov, V. N.; Kobayashi, R.; Normand, J.; Raghavachari, K.; Rendell, A. P.; Burant, J. C.; Iyengar, S. S.; Tomasi, J.; Cossi, M.; Rega, N.; Millam, N. J.; Klene, M.; Knox, J. E.; Cross, J. B.; Bakken, V.; Adamo, C.; Jaramillo, J.; Gomperts, R.; Stratmann, R. E.; Yazyev, O.; Austin, A. J.; Cammi, R.; Pomelli, C.; Ochterski, J. W.; Martin, R. L.; Morokuma, K.; Zakrzewski, V. G.; Voth, G. A.; Salvador, P.; Dannenberg, J. J.; Dapprich, S.; Daniels, A. D.; Farkas, Ö.; Foresman, J. B.; Ortiz, J. V.; Cioslowski, J.; Fox, D. J. *Gaussian 03*; Gaussian, Inc.: Wallingford, CT, USA, 2004.
(38) Breneman, C. M.; Wiberg, K. B. Determining atom-centered monopoles from molecular electrostatic potentials. The need for high sampling density in formamide conformational analysis. *J. Comput. Chem.* **1990**, *11*, 361−373.
(39) Tieleman, D. P.; MacCallum, J. L.; Ash, W. L.; Kandt, C.; Xu, Z.; Monticelli, L. Membrane protein simulations with a united-atom lipid and all-atom protein model: lipid−protein interactions, side chain transfer free energies and model proteins. *J. Phys.: Condens. Matter* **2006**, *18*, S1221.
(40) Jorgensen, W. L.; Chandrasekhar, J.; Madura, J. D.; Impey, R. W.; Klein, M. L. Comparison of simple potential functions for simulating liquid water. *J. Chem. Phys.* **1983**, *79*, 926−935.
(41) Hess, B.; Bekker, H.; Berendsen, H. J. C.; Fraaije, J. G. E. M. LINCS: a linear constraint solver for molecular simulations. *J. Comput. Chem.* **1997**, *18*, 1463−1472.
(42) Hess, B. P-LINCS: A parallel linear constraint solver for molecular simulation. *J. Chem. Theory Comput.* **2008**, *4*, 116−122.
(43) Darden, T.; York, D.; Pedersen, L. Particle mesh Ewald: An N log (N) method for Ewald sums in large systems. *J. Chem. Phys.* **1993**, *98*, 10089−10092.
(44) Essmann, U.; Perera, L.; Berkowitz, M. L.; Darden, T.; Lee, H.; Pedersen, L. G. A smooth particle mesh Ewald method. *J. Chem. Phys.* **1995**, *103*, 8577−8593.

DOI: 10.1021/acs.langmuir.8b00372
Langmuir 2018, 34, 4314−4323

(45) Verlet, L. Computer "Experiments" on Classical Fluids. I. Thermodynamical Properties of Lennard-Jones Molecules. *Phys. Rev.* **1967**, *159*, 98−103.
(46) Páll, S.; Hess, B. A flexible algorithm for calculating pair interactions on SIMD architectures. *Comput. Phys. Commun.* **2013**, *184*, 2641−2650.
(47) Berendsen, H. J. C.; Postma, J. P. M.; van Gunsteren, W. F.; DiNola, A.; Haak, J. R. Molecular dynamics with coupling to an external bath. *J. Chem. Phys.* **1984**, *81*, 3684−3690.
(48) Bussi, G.; Donadio, D.; Parrinello, M. Canonical sampling through velocity rescaling. *J. Chem. Phys.* **2007**, *126*, 014101.
(49) Parrinello, M.; Rahman, A. Polymorphic transitions in single crystals: A new molecular dynamics method. *J. Appl. Phys.* **1981**, *52*, 7182−7190.
(50) Nosé, S.; Klein, M. L. Constant pressure molecular dynamics for molecular systems. *Mol. Phys.* **1983**, *50*, 1055−1076.
(51) Shirts, M. R.; Chodera, J. D. Statistically optimal analysis of samples from multiple equilibrium states. *J. Chem. Phys.* **2008**, *129*, 124105.
(52) Shirts, M. R.; Pitera, J. W.; Swope, W. C.; Pande, V. S. Extremely precise free energy calculations of amino acid side chain analogs: Comparison of common molecular mechanics force fields for proteins. *J. Chem. Phys.* **2003**, *119*, 5740−5761.
(53) Klimovich, P. V.; Mobley, D. L. A. Python tool to set up relative free energy calculations in GROMACS. *J. Comput.-Aided Mol. Des.* **2015**, *29*, 1007−1014.
(54) Oplawski, S. M. *Extraction of indicator dyes into imidazolium-based ionic liquids*; The University of Wisconsin-Milwaukee, 2014.
(55) da Silva, J. S.; Junqueira, H. C.; Ferreira, T. L. Effect of pH and dye concentration on the n-octanol/water distribution ratio of phenothiazine dyes: a microelectrode voltammetry study. *Electrochim. Acta* **2014**, *144*, 154−160.
(56) Wainwright, M.; Phoenix, D. A.; Marland, J.; Wareing, D. R. A.; Bolton, F. J. A study of photobactericidal activity in the phenothiazinium series. *FEMS Immunol. Med. Microbiol.* **1997**, *19*, 75−80.
(57) Wagner, S. J.; Skripchenko, A.; Robinette, D.; Foley, J. W.; Cincotta, L. Factors affecting virus photoinactivation by a series of phenothiazine dyes. *Photochem. Photobiol.* **1998**, *67*, 343−349.
(58) Walker, I.; Gorman, S. A.; Cox, R. D.; Vernon, D. I.; Griffiths, J.; Brown, S. B. A comparative analysis of phenothiazinium salts for the photosensitisation of murine fibrosarcoma (RIF-1) cells in vitro. *Photochem. Photobiol. Sci.* **2004**, *3*, 653−659.
(59) Thomas, D. S.; Hossack, J. A.; Rose, A. H. Plasma-membrane lipid composition and ethanol tolerance in Saccharomyces cerevisiae. *Arch. Microbiol.* **1978**, *117*, 239−245.
(60) Kozaki, A.; Watanabe, J. Distribution of methylene blue and chlordiazepoxide in rabbits. *J. Pharmacobio-Dyn.* **1979**, *2*, 37−44.
(61) Kohlmeyer, A. *Topotools* 2017, DOI: 10.5281/zenodo.545655.
(62) Tironi, I. G.; Sperb, R.; Smith, P. E.; Gunsteren, W. F. V. A generalized reaction field method for molecular dynamics simulations. *J. Chem. Phys.* **1995**, *102*, 5451−5459.
(63) van Der Spoel, D.; van Maaren, P. J. The origin of layer structure artifacts in simulations of liquid water. *J. Chem. Theory Comput.* **2006**, *2*, 1−11.
(64) Conn, H. J.; Lillie, R. D. *HJ Conn's Biological Stains*; Williams & Wilkins, 1977.
(65) Bancroft, J. D.; Gamble, M. *Theory and Practice of Histological Techniques*; Elsevier Health Sciences, 2008.
(66) Buchholz, K.; Schirmer, R. H.; Eubel, J. K.; Akoachere, M. B.; Dandekar, T.; Becker, K.; Gromer, S. Interactions of Methylene Blue with Human Disulfide Reductases and Their Orthologues from Plasmodium falciparum. *Antimicrob. Agents Chemother.* **2008**, *52*, 183−191.
(67) Kučerka, N.; Nagle, J. F.; Sachs, J. N.; Feller, S. E.; Pencer, J.; Jackson, A.; Katsaras, J. Lipid Bilayer Structure Determined by the Simultaneous Analysis of Neutron and X-Ray Scattering Data. *Biophys. J.* **2008**, *95*, 2356−2367.
(68) Pan, J.; Tristram-Nagle, S.; Kučerka, N.; Nagle, J. F. Temperature Dependence of Structure, Bending Rigidity, and Bilayer Interactions of Dioleoylphosphatidylcholine Bilayers. *Biophys. J.* **2008**, *94*, 117−124.
(69) Liu, Y.; Nagle, J. F. Diffuse scattering provides material parameters and electron density profiles of biomembranes. *Phys. Rev. E: Stat., Nonlinear, Soft Matter Phys.* **2004**, *69*, 040901.
(70) Tristram-Nagle, S.; Petrache, H. I.; Nagle, J. F. Structure and Interactions of Fully Hydrated Dioleoylphosphatidylcholine Bilayers. *Biophys. J.* **1998**, *75*, 917−925.
(71) Kučerka, N.; Gallová, J.; Uhríková, D.; Balgavý, P.; Bulacu, M.; Marrink, S.-J.; Katsaras, J. Areas of Monounsaturated Diacylphosphatidylcholines. *Biophys. J.* **2009**, *97*, 1926−1932.
(72) Attwood, S.; Choi, Y.; Leonenko, Z. Preparation of DOPC and DPPC supported planar lipid bilayers for atomic force microscopy and atomic force spectroscopy. *Int. J. Mol. Sci.* **2013**, *14*, 3514−3539.
(73) Nagle, J. F.; Tristram-Nagle, S. Structure of lipid bilayers. *Biochim. Biophys. Acta, Rev. Biomembr.* **2000**, *1469*, 159−195.
(74) Filippov, A.; Orädd, G.; Lindblom, G. Influence of Cholesterol and Water Content on Phospholipid Lateral Diffusion in Bilayers. *Langmuir* **2003**, *19*, 6397−6400.
(75) Weber, G.; Charitat, T.; Baptista, M. S.; Uchoa, A. F.; Pavani, C.; Junqueira, H. C.; Guo, Y.; Baulin, V. A.; Itri, R.; Marques, C. M.; Schroder, A. P. Lipid oxidation induces structural changes in biomimetic membranes. *Soft Matter* **2014**, *10*, 4241−4247.

DOI: 10.1021/acs.langmuir.8b00372
Langmuir 2018, 34, 4314−4323